



Modelling three-dimensional flow over spur-and-groove morphology

Renan F. da Silva^{1,2,3,4}  · Curt D. Storlazzi⁵ · Justin S. Rogers⁶ · Johan Reynolds^{1,7} · Robert McCall¹

Received: 28 January 2020 / Accepted: 29 September 2020 / Published online: 19 October 2020
© Crown 2020

Abstract Spur-and-groove (SAG) morphology characterizes the fore reef of many coral reefs worldwide. Although the existence and geometrical properties of SAG have been well documented, an understanding of the hydrodynamics over them is limited. Here, the three-dimensional flow patterns over SAG formations, and a sensitivity of those patterns to waves, currents, and SAG geometry were characterized using the physics-based Delft3D-FLOW and SWAN models. Shore-normal shoaling waves over SAG formations were shown to drive two circulation cells: a cell on the lower fore reef with offshore flow over the spurs and

onshore flow over the grooves, except near the seabed where velocities were always onshore, and a cell on the upper fore reef with offshore surface velocities and onshore bottom currents, which result in depth-averaged onshore and offshore flow over the spurs and grooves, respectively. The mechanism driving this flow results from the net of the radiation stress gradients and pressure gradient, which is balanced by the Reynolds stress gradients and bottom friction that differ over the spur and over the groove. Waves were the primary driver of variations in modelled flow over SAG, with the flow strength increasing for increasing wave heights and periods. Spur height, SAG wavelength, and the water depth at peak spur height were the dominant influences on the hydrodynamics, with spur heights directly proportional to the strength of SAG circulation cells. SAG formations with shorter SAG wavelengths only presented one circulation cell on the shallower portion of the reef, as opposed to the two circulation cells for longer SAG wavelengths. SAG formations with peak spur heights occurring in shallower water had stronger circulation than those with peak spur heights occurring in deeper water. These hydrodynamic patterns also likely affect coral and reef development through sediment and nutrient fluxes.

Topic Editor Mark R. Patterson

Electronic supplementary material The online version of this article (<https://doi.org/10.1007/s00338-020-02011-8>) contains supplementary material, which is available to authorized users.

✉ Renan F. da Silva
renan.silva@research.uwa.edu.au

- ¹ Deltares, P.O Box 177, 2600 MH Delft, The Netherlands
- ² School of Earth Sciences and UWA Oceans Institute, The University of Western Australia, 35 Stirling Highway, Crawley, WA 6009, Australia
- ³ ARC Centre of Excellence for Coral Reef Studies, The University of Western Australia, 35 Stirling Highway, Crawley, WA 6009, Australia
- ⁴ Wave Energy Research Centre, The University of Western Australia, 35 Stirling Highway, Crawley, WA 6009, Australia
- ⁵ U.S. Geological Survey, Pacific Science Center, 2885 Mission Street, Santa Cruz, CA 95060, USA
- ⁶ Department of Civil and Environmental Engineering, Stanford University, Y2E2, 473 Via Ortega, Stanford, CA 94305, USA
- ⁷ Water Science and Engineering, IHE Delft, Westvest 7, 2611 AX Delft, The Netherlands

Keywords Coral reef · Spur-and-groove · Waves · Currents · (3D) modelling · Delft3D

Introduction

Spur-and-groove (SAG) morphology is a common and impressive characteristic of coral reefs worldwide. It is composed of a series of submerged shore-normal coral ridges (spurs) separated by shore-normal patches of

sediment (grooves), starting at the seawards edge of the reef flat extending down the reef slope into deeper water (Guilcher 1988). SAG morphology has been observed along fringing reefs, barrier reefs, and atolls in the Pacific Ocean (Munk and Sargent 1948; Storlazzi et al. 2003), the Atlantic Ocean (Shinn et al. 1981), the Indian Ocean (Weydert 1979; Bouchon 1981), Caribbean Sea (Goreau 1959; Blanchon and Jones 1997), and the Red Sea (Sneh and Friedman 1980). The geometric properties of SAG formations have been described by numerous authors (Munk and Sargent 1948; Storlazzi et al. 2003). Duce et al. (2016) observed that there is no standard definition of morphometric parameters, and authors report different metrics. This manuscript adopts the measurable morphometric parameters for the SAG geometric description shown in Fig. 1 and Table 1, predominantly using the same terminologies as Storlazzi et al. (2003) and Rogers et al. (2013). Rogers et al. (2013) noted that although the scales of SAG vary worldwide, spur heights are on the order of 0.5–10 m, SAG alongshore wavelength (i.e., the distance between adjacent spur peaks) on the order of 5–150 m, and

groove widths on the order of 1–100 m. SAG structures can be found in depths ranging from 0 to 45 m (Wood and Oppenheimer 2000).

The importance of SAG structures is related to their potential role as regulators of hydraulic energy, sediment, and nutrients given (a) their location between the reef flat and deep ocean, and (b) the fact that they generally host the corals with growth rates faster than the rest of the reef (Munk and Sargent 1948; Odum and Odum 1955). Regardless of their location in the reef profile (e.g., in the SAG zone or in the reef flat), coral reefs seem more prone to develop in environments with an ideal range of hydrodynamic conditions (e.g., Storlazzi et al. 2003, 2005). Energetic environments might limit reef development, as extreme waves could break them or induce high abrasion by bedload and suspended sediment concentrations, which are usually understood as factors with the potential to harm coral health (Dollar 1982; Storlazzi et al. 2003, 2005). On the other hand, increasing water motion may induce more mass transfer and nutrient uptake, enhancing photosynthetic production (Falter et al. 2004; Rogers et al. 2013).

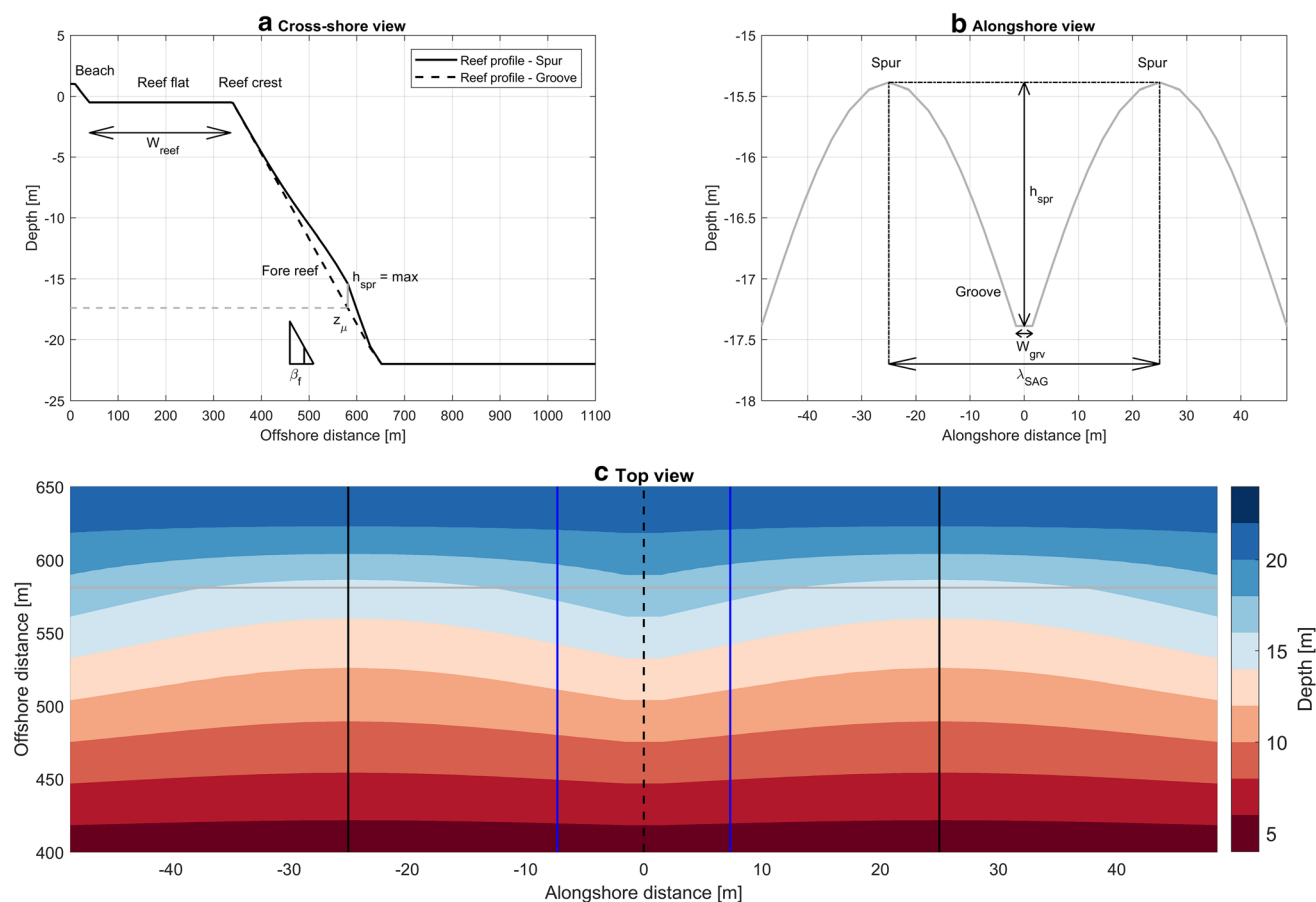


Fig. 1 Schematic views of spur-and-groove morphology as represented in the modelling (base case). **a** Cross-shore view. **b** Alongshore view. **c** Map/top view. Solid black line represents the cross-shore axis of the spur, and dashed black line is the cross-shore axis of the

groove. The blue lines are mid positions between spur and groove. The grey line is the alongshore axis where spur height is greatest along the cross-shore profile. The coloured gradations represent depth

Table 1 Range of parameter: waves, currents, and spur-and-groove geometry

Type	Variable	Symbol	Range of values (base case)	Unit
Wave parameters	Significant wave height	H_{S0}	0.5–6 (1)	m
	Wave steepness*	$H_{S0} L_{p0}^{-1}$	0.006–0.050 (0.006)	–
	Spur height	h_{spr}	0.5–8.0 (2)	m
SAG geometry	Spur-and-groove wavelength	λ_{SAG}	25–100 (50)	m
	Ratio of groove width and SAG wavelength	$W_{grv} \lambda_{SAG}^{-1}$	0.01–0.82 (0.06)	–
	SAG cross-shore slope	$\tan \beta_f$	0.02–0.50 (0.07)	–
	Reef flat width	W_{reef}	50–1000 (300)	m
	Ratio of friction coefficient between groove and spur	$C_{D-groove} C_{D-spur}^{-1}$	1/6–0.5 (0.5)	–
	Vertical position of maximum spur height	z_{μ}	5–17 (17)	m
Alongshore forcing	Alongshore wind speed	U_{10}	0–20 (0)	$m s^{-1}$

*The equivalent peak wave period lies in the range of 3–15 s (10 s for the base case)

SAG formations are more commonly found in wave-dominated environments and numerous studies have related the SAG geometry to the incident wave conditions (Munk and Sargent 1948; Storlazzi et al. 2003; Rogers et al. 2013). SAG formations are prone to develop in more exposed areas (Munk and Sargent 1948; Duce et al. 2014), and spur alignment is generally considered to be orthogonal to the direction of the main incoming wave (Shinn 1963; Duce et al. 2016). Storlazzi et al. (2003) and Duce et al. (2016) noted that SAG wavelengths tend to be shorter both for more exposed and shallower areas. As more exposed and shallower locations are generally characterized by greater wave energy, these trends suggest that wave energy is associated with SAG morphology, with higher energy areas tending to have closer groove spacing (or shorter SAG wavelengths).

Although the existence and geometrical properties of SAG are well documented, the literature concerning specifically the hydrodynamics around them is sparse. Rogers et al. (2013) investigated the hydrodynamics of SAG with a two-dimensional Boussinesq-type model and identified a nearshore Lagrangian circulation pattern of counter-rotating circulation cells, with transport offshore over the spur and onshore over the groove on the lower fore reef of the SAG, and with the reversed pattern on the upper fore reef. The only known extensive set of field data

collected in SAG formations was made by Rogers et al. (2015) on Palmyra Atoll, where measurements of velocities and pressures on top of spur and grooves at depths around 10 m were made. Their measurements showed the existence of situations with circulation cells, whose strength increased for hydrodynamic conditions with directly incident wave direction and low alongshore flow.

Despite the initial efforts to investigate the hydrodynamics over SAG morphology, to date no research has tackled the three-dimensional (3D) wave-driven flow pattern over SAG morphology, and the influence of the 3D flow effects on coral development remains unknown. To address this gap, we described the 3D circulation found within SAG formations and investigated the sensitivity of these patterns to waves, alongshore currents, and SAG geometry parameters by means of physics-based numerical model simulations. The ultimate objective of this work is to provide scientists predictive capability of the flow regime for a range of conditions commonly found on coral reefs with SAG formations. Furthermore, we discuss the implications of the hydrodynamic aspects for corals and nutrient and sediment transport in the context of coral health and growth.

Methods

Three-dimensional wave-averaged model

We used numerical modelling to provide a full characterization of the 3D wave-driven flow patterns over SAG structures. An extensive set of simulations was used to describe the circulation patterns found within SAG formations and to identify their governing mechanisms. Delft3D (D3D) is a fully integrated computer software suite for 3D computations for coastal and estuarine areas (Lesser et al. 2004). The D3D suite is composed of several modules, and in this work the coupling between D3D-FLOW version 3.59.01.48550 (Lesser et al. 2004) and SWAN version 40.72 (Booij et al. 1999) were used for all the simulations. In D3D-FLOW, the generalized Lagrangian mean (GLM) formulation is used to solve the shallow water momentum equations (Andrews and McIntyre 1978), namely the wave-averaged (i.e., time-averaged over many wave periods) mass- and momentum-balance equations. SWAN uses the wave action balance equation to calculate the propagation of wave fields over space and receives from D3D-FLOW the mean flow conditions (e.g., water levels). With the wave energy obtained over the entire domain, the wave forces (i.e., radiation stress gradients), which are calculated with linear wave theory expressions, are coupled back as an additional force to the flow computation (see Lesser et al. 2004, for more details).

Parameter space

We first defined a base case scenario (Table 1), and then we investigated the sensitivity of the flow due to each of the parameters: waves, SAG geometry, alongshore flow, hereafter referred to as sensitivity runs. The base case, with bathymetry shown in Fig. 1, corresponds to a typical SAG formation found in southern Moloka'i, as described by Storlazzi et al. (2003) and Rogers et al. (2013). The sensitivity runs are the same as the base case run, except for the varying parameters that were changed one at a time. The sensitivity runs allowed the identification of the parameters with greatest influence on the flow patterns. In the second step, those parameters were varied simultaneously so as to best understand the variation in, and controls on, flows over SAG formations.

The range of parameters simulated is presented in Table 1 and discussed below. Of the wave parameters, the incident significant wave height, H_{s0} , and the wave steepness, $H_{s0}L_{p0}^{-1}$, where L_{p0} is the peak wavelength in deep water, were varied, whereas only shore-normal waves were investigated for simplicity. The range of values used here took into consideration parameter variation reported in

previous research both specifically on SAG hydrodynamics (Rogers et al. 2013) and on coral reefs (Quataert et al. 2015; Lowe and Falter 2015).

To represent the vast variation of SAG formations, we used schematic bathymetries and friction in the modelling (see Appendix 1 and Fig. 1). The SAG geometry considers the following set of SAG geometric parameters: spur height (h_{spr}), spur wavelength (λ_{SAG}), ratio of groove width to spur wavelength ($W_{grv} \lambda_{SAG}^{-1}$), cross-shore slope (β_f), reef flat width (W_{ref}), the ratio of friction coefficient between the spurs and grooves ($C_{D-grv} C_{D-spr}^{-1}$; see Appendix 1) and vertical position of maximum spur height (z_μ) (Fig. 1). The choice of the range of these parameters considered sets of SAG geometries reported in numerous research publications (Goreau 1959; Shinn et al. 1981; Storlazzi et al. 2003; Rogers et al. 2013; Quataert et al. 2015; Duce et al. 2016).

To identify how the 3D circulation over SAG bathymetries changes with alongshore forcing, the alongshore wind speed was selected to drive alongshore currents. A range of wind speeds was applied, with maximum value of 20 m s^{-1} that corresponds to storm conditions.

Model set-up

The model grid for the base case scenario is shown in Supplementary Fig. 1. A total of 14 SAG formations were included in each bathymetry; results were only retained in the central SAG formations to remove domain edge effects. The alongshore resolution over the SAG varied from 50 m outside the SAG zone down to 1/3 of the groove width in the groove (1 m for the base case). The cross-shore resolution varied from 25 m at the offshore extent of the model to 3 m near the reef crest. Twenty sigma-layers were used in the vertical, with finer grids close to the bottom and to the water surface. In a depth of 22 m, the smallest and largest grid spacings were 6 cm and 4.2 m in the bottom/surface layers and in mid-depth, respectively.

The model settings for D3D-FLOW and SWAN are summarized in Supplementary Table 1. In this work, we hypothesized that the combined effect of refraction and diffraction occurring over SAG formations could be represented in SWAN by neglecting them both (note that wave-averaged models like SWAN do not account for diffraction as part of their core equation). This hypothesis was grounded upon the results found by Rogers et al. (2013), which suggested that the combined effect of refraction and diffraction is close to null for SAG formations with limited SAG wavelengths ($\lambda_{SAG} \leq 100 \text{ m}$). We validated this assumption by comparing our model results with a wave-resolving model (see Appendix 2).

Results

First, we studied in detail the base case model results (section “**Base case**”), which were found to be representative for the majority of the simulated conditions. Next, we presented the mechanisms and effects of varying conditions on the velocity profile (section “**Changes to the velocity profiles**”).

Base case

Wave propagation and water levels

Waves approaching the SAG zone were found to first gradually shoal on the lower fore reef (here defined as zone of the reef with depths larger than approximately 12 m) and then started shoaling quickly on the upper fore reef up to the point where they broke onshore of the SAG zone and before the reef crest. The waves’ heights rapidly decreased

over the reef crest and then continued to decrease over the reef flat (Fig. 2a). The common set-down/set-up pattern (e.g., Buckley et al. 2015) for sloping reefs was reproduced: on the lower fore reef, the mean water level η (Fig. 2b) decreased (set-down) and continued decreasing on the upper fore reef until the break point, where it attained its minimum value. From that point farther onshore, an increase of η (set-up) occurred, it increased most rapidly where the wave breaking was greater, and then it increased more gradually, reaching a maximum value at the shoreline.

Velocity profiles

The Lagrangian cross-shore currents (note that all currents referred to hereafter are Lagrangian, except where indicated) were found to be dominant over the alongshore and vertical velocities; thus, only the cross-shore velocities were explored in detail. First, all currents (Fig. 3a) had

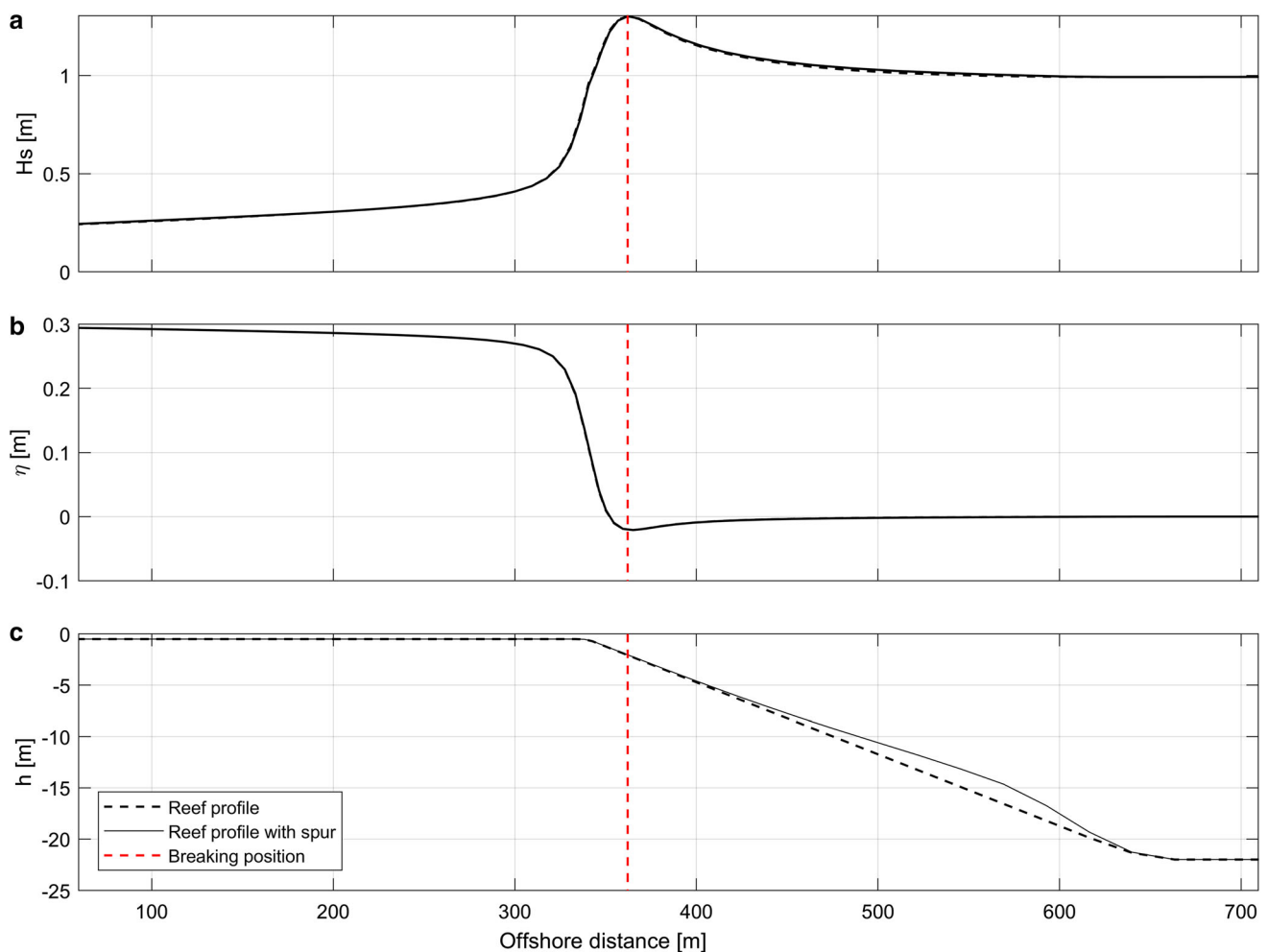


Fig. 2 Cross-shore variations in waves and water level over spur-and-groove morphology for base case. **a** Significant wave height, H_s . **b** Mean water level, η . **c** Depth profile over spurs (solid lines) and grooves (dashed lines), h . The red dashed line provides the wave-breaking position

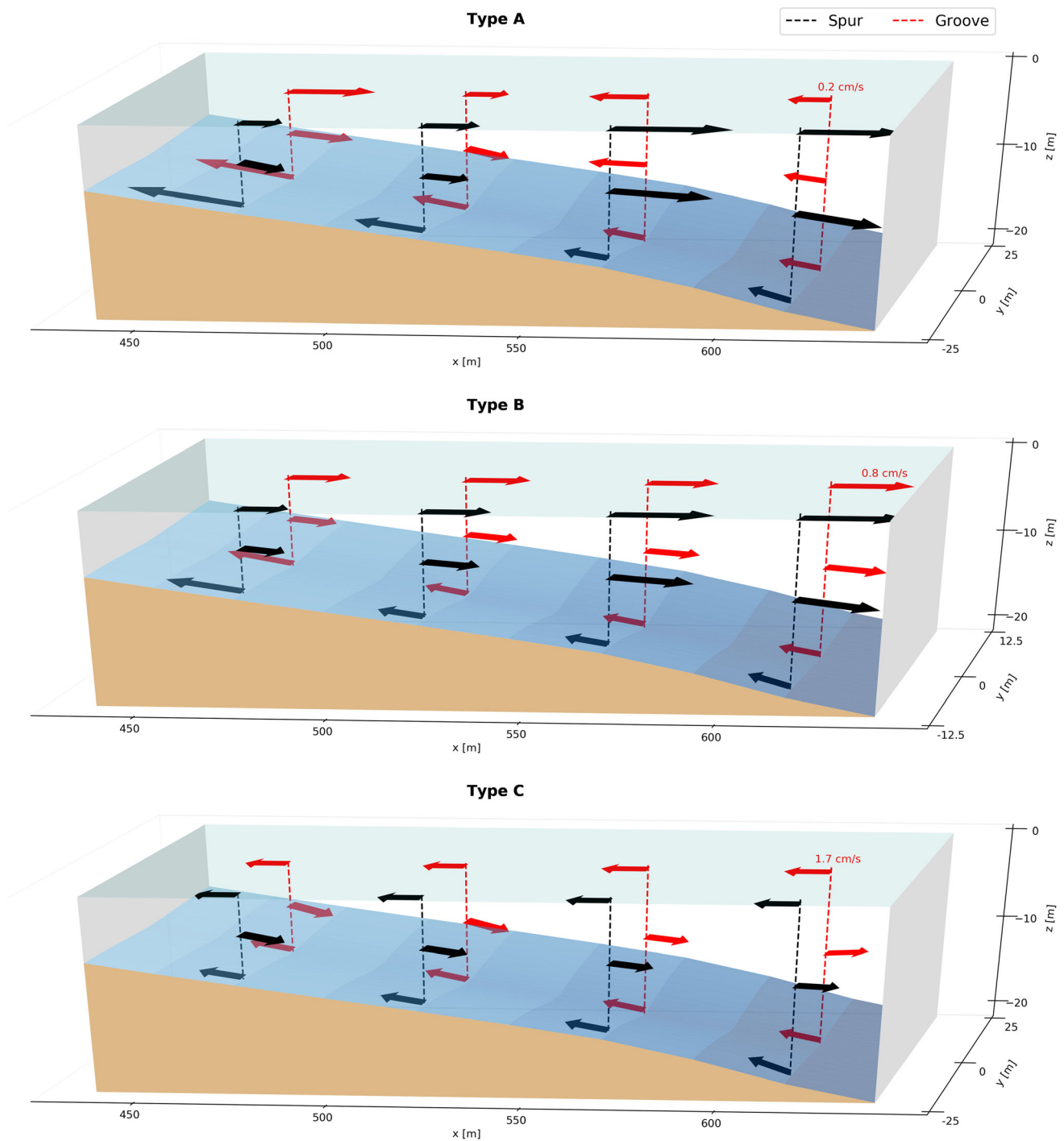


Fig. 3 Types of flow pattern over the spur (black) and groove (red). **a** Type A (base case). **b** Type B (with spur-and-groove wavelength λ_{SAG} of 25 m). **c** Type C (with $Hs_0Lp_0^{-1}$ of 0.025). Arrows indicate Lagrangian velocity (u_L , w_L)

relatively low magnitudes, on the order of $1\text{--}10\text{ cm s}^{-1}$. On the lower fore reef over the grooves, currents were onshore, whereas over the spurs they were predominantly offshore, becoming onshore only close to the seafloor (i.e., roughly the lowest 3 m). Approaching the surf zone (depths = 5 m), the velocity profiles over both spur and groove showed offshore surface currents and onshore

bottom velocities. Depth-averaged flow in the groove was offshore, since offshore surface currents were faster than the onshore bottom velocities. As for the spur, the onshore bottom currents were faster than the offshore surface currents, yielding depth-averaged flow in the onshore direction (not shown).

The surface streamlines indicated that surface tracers over the SAG would tend to flow offshore through the spurs, except for the groove on the lower fore reef, where they had closed elliptical paths (Fig. 4a). Bottom shear stress (i.e., the wave-averaged bottom shear stresses that include contribution from waves) values in the SAG zone were on the order of 0.1 Pa, being higher over the spurs than over grooves (Fig. 4b). A similar order of magnitude of shear stresses with higher values over spurs was also found for SAG formations on Palmyra Atoll (Rogers et al. 2015). The bottom currents were onshore everywhere in the SAG zone (Fig. 4c), indicating that bottom tracers would flow onshore.

The alongshore and vertical velocities were lower than the cross-shore currents (Fig. 5), and the cross-shore vorticity was concentrated near the bed (Supplementary Fig. 3a–c). The flow converged towards the higher portion of the water column over the groove in the lower fore reef (Fig. 5a), whereas approaching the transition between lower and upper fore reef (Fig. 5b), it focused towards the near-bed over the spur. The upper fore reef (Fig. 5c) was

characterized by a dominance of vertical velocities over alongshore velocities.

Momentum balance

To investigate the mechanisms for the SAG circulation, we conducted the momentum balance analysis (see momentum terms in Eq. (4) of Lesser et al. 2004) in the cross-shore over the spur and the groove (Fig. 6). The wave force and pressure gradient were the dominant forces, and, as they were nearly in balance, the set-down pattern was observed in the SAG zone. The net of wave force and pressure gradient, which is the driver of currents, was primarily balanced by the Reynolds stress horizontal and vertical gradients, as well as bottom friction. The remaining momentum terms (i.e., acceleration terms) were found to be negligible. Over the groove, the net of the wave force and pressure gradient was directed onshore (i.e., the onshore pressure gradient exceeded the offshore wave force) on the lower fore reef and became offshore in the upper fore reef. Over the spur, the net of the wave force and pressure gradient was nearly always directed offshore. The

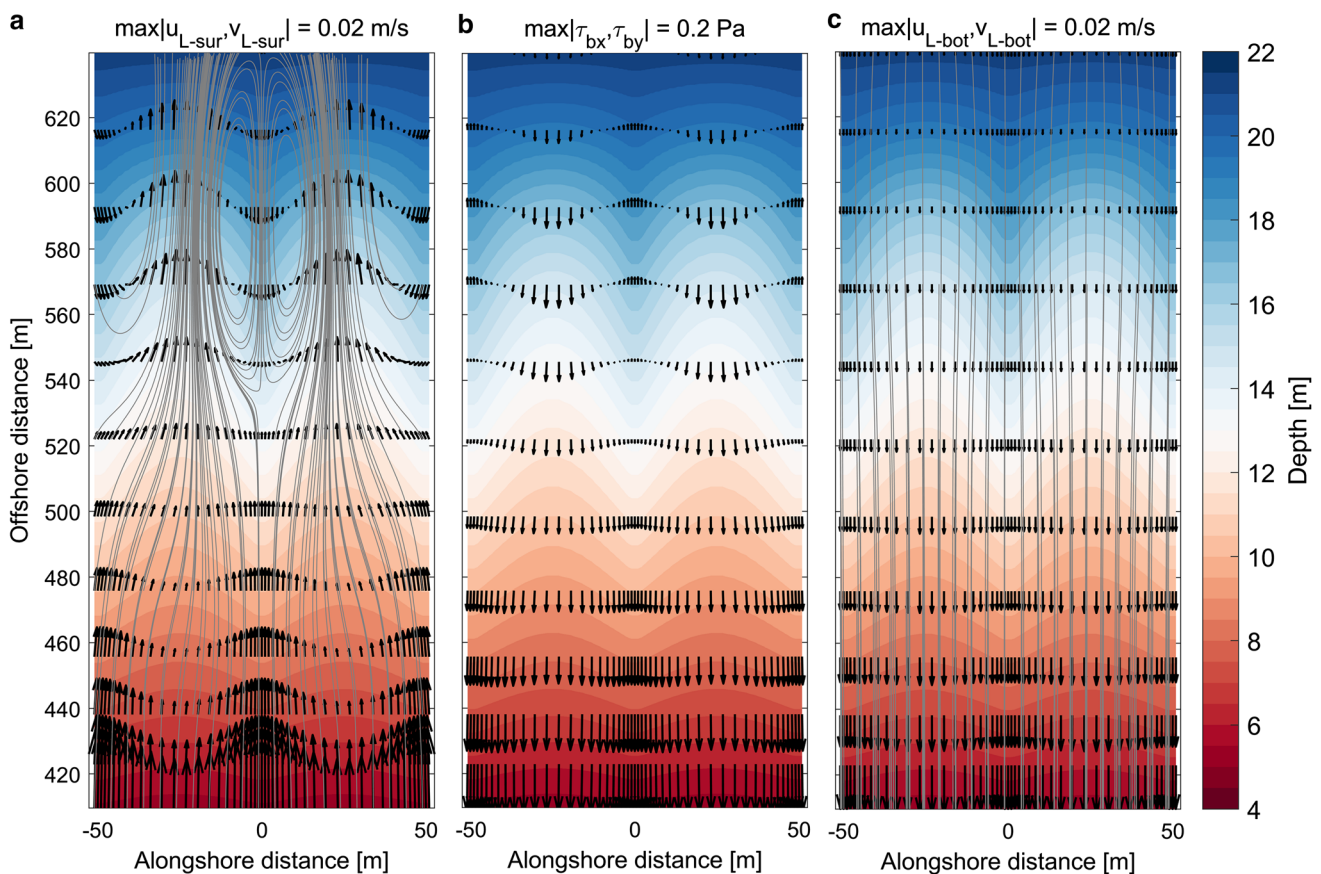


Fig. 4 Map view of near-surface (averaged over the top 0.5 m) and near bed (averaged over the lowest 0.5 m). **a** Cross-shore, u_{L-sur} , and alongshore, v_{L-sur} , Lagrangian surface velocities (arrows), with

streamlines (grey lines). **b** Cross-shore, τ_{bx} , and alongshore, τ_{by} , bottom shear stresses. **c** Cross-shore, u_{L-bot} , and alongshore, v_{L-bot} , Lagrangian bottom velocities (arrows), with streamlines (grey lines)

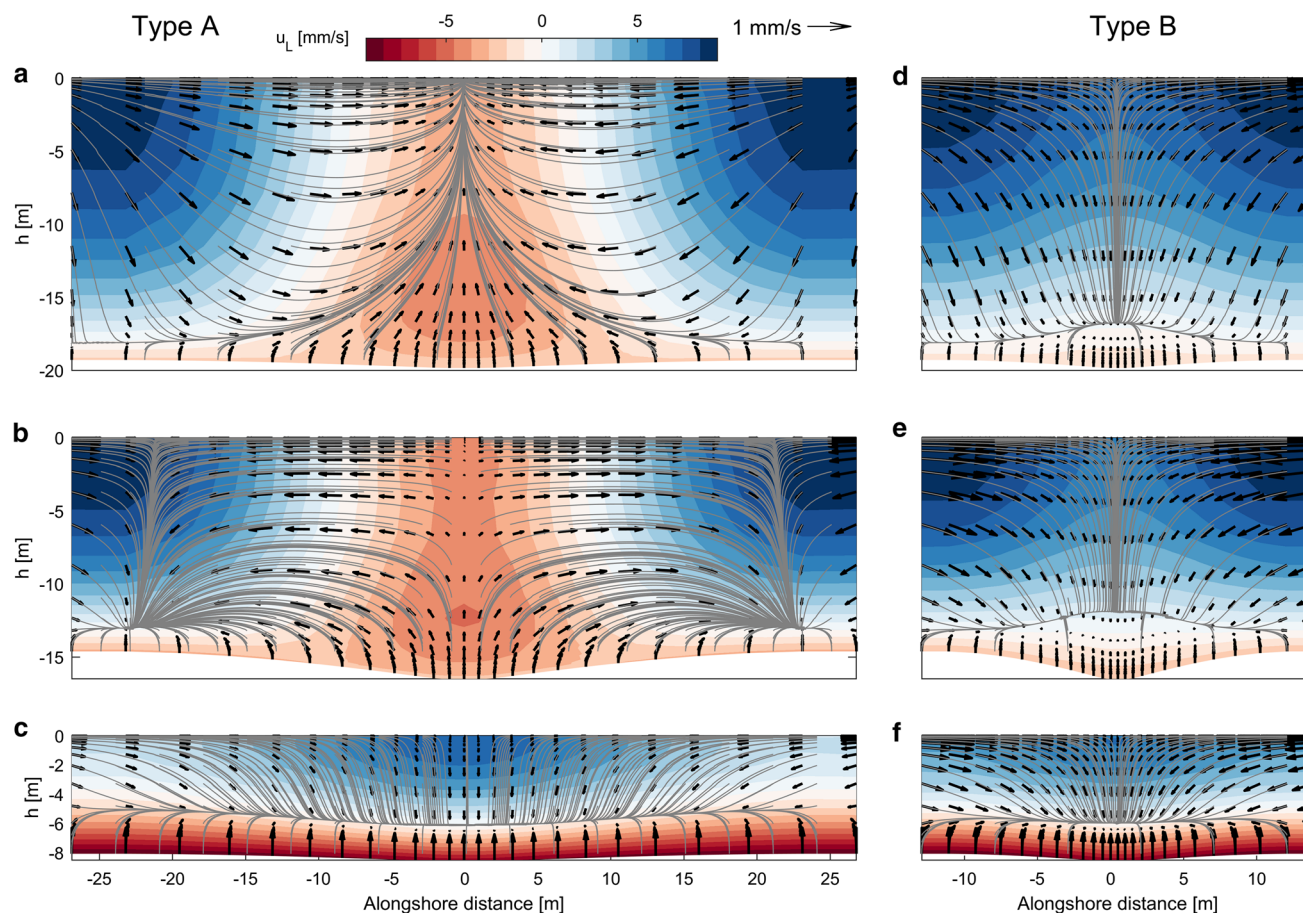


Fig. 5 Alongshore view of Lagrangian velocity, u_L (colour, + blue is offshore and - red is onshore flow), v_L and w_L (arrows) with streamlines (grey lines), for Types A (left)—base case—, and B (right)—with spur-and-groove wavelength λ_{SAG} of 25 m—for 3

different alongshore sections. **a** Type A, depth of 20 m. **b** Type A, depth of 16 m. **c** Type A, depth of 9 m. **d** Type B, depth of 20 m. **e** Type B, depth of 16 m. **f** Type B, depth of 9 m

reversal of the depth-averaged currents over the groove occurred in the location where pressure gradient nearly equaled wave force.

Changes to the velocity profiles

Mechanisms and effects

To investigate the effects of variations of wave parameters, SAG geometry, and alongshore forcing, we studied the cross-shore velocity profiles on top of spurs and grooves for the sensitivity runs (Fig. 7; note that for brevity we show the results only for a few parameters, albeit a similar analysis was performed for all other parameters; see Silva 2017). Next, we estimated the changes to the overall strength of the flow by comparing the normalized maximum depth-averaged velocity over the spur (Fig. 8; note that the analysis with normalized near-surface and near-bottom velocities, which were also conducted and are not presented here for brevity, showed the same trends as the

depth-averaged velocities). We also investigated situations in which alongshore currents were dominant by estimating the ratio of the spatial mean of the absolute depth-averaged alongshore and cross-shore currents (Supplementary Fig. 4). To understand the mechanisms for the changes to the hydrodynamics, we calculated the spatial mean of the absolute depth-integrated momentum terms (Supplementary Fig. 5). The dominant effects and associated mechanisms in the cross-shore velocity profile due to changing forcing conditions and SAG characteristics are summarized in Table 2.

Wave heights were the primary control on flow strength (Fig. 7a). Larger waves induced significantly stronger circulation cells (Fig. 8a), primarily due to the higher wave forcing involved in the momentum balance that led to an overall growing of the remaining balancing terms (i.e., pressure gradient, Reynolds stress gradients, acceleration and bottom friction; Supplementary Fig. 5a). When waves started breaking due to depth limitation (e.g., Fig. 2a), the SAG circulation cell decayed, and the velocity profile

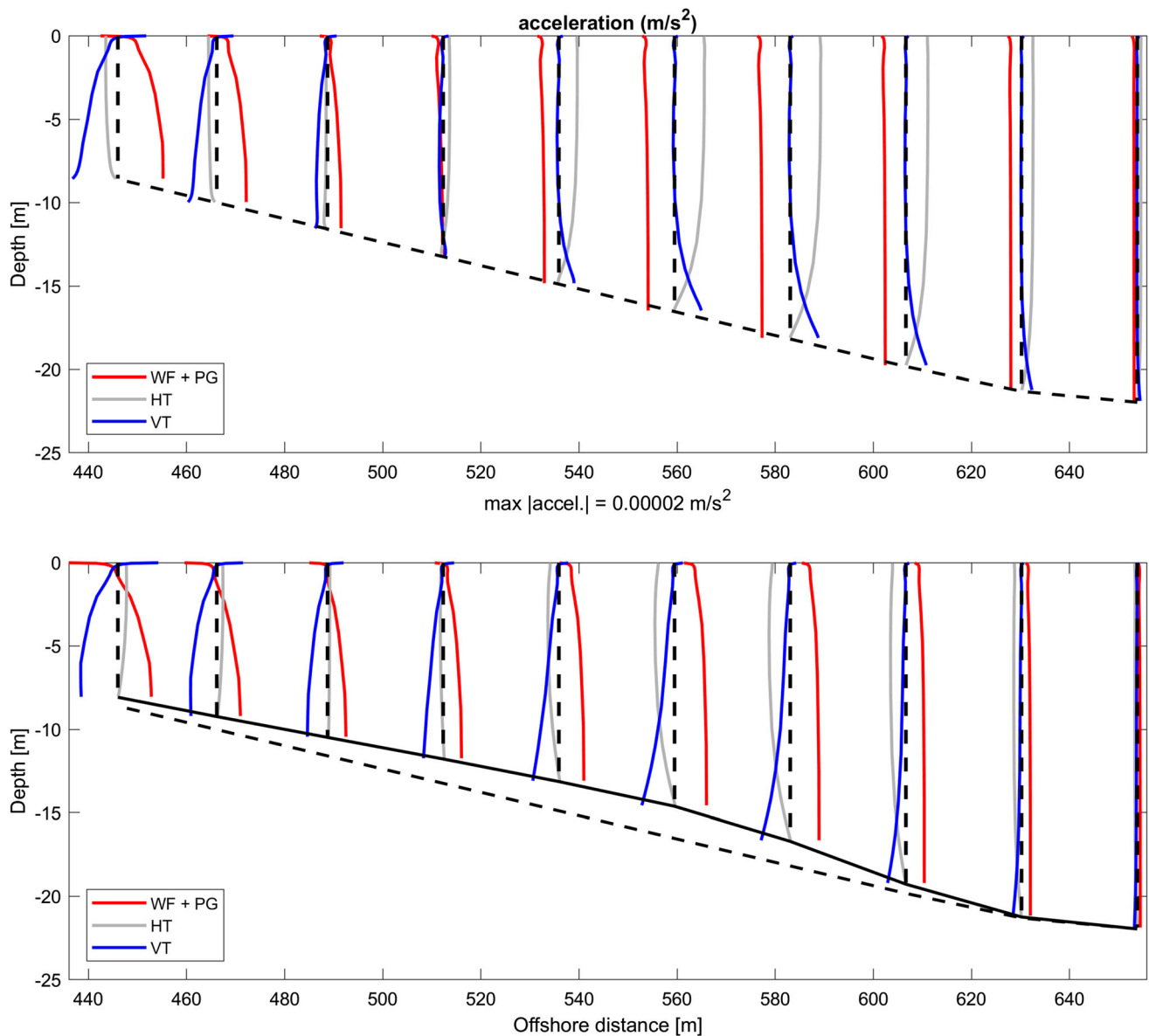


Fig. 6 Cross-shore variations in the momentum terms over the groove (top) and spur (bottom). The horizontal black lines represent the bottom profile (solid for spur and dashed for groove). The vertical black lines indicate the positions where the momentum terms are plotted, thus with null momentum terms. The momentum terms are wave force (WF), pressure gradient (PG), Reynolds stress horizontal gradients (HT), and Reynolds stress vertical gradients (VT). The local

and advective accelerations were found to be negligible. We did not show the results at the bottom layer, where bottom friction is relevant, for scaling purposes. Note that the Reynolds stress vertical gradients were assumed to be equal to the residual (i.e., the sum of all momentum terms), as D3D-FLOW provides output for all momentum terms, except for them and for the vertical advective terms, and with scale analysis we assumed the last to be much smaller than the former

shape started developing onshore surface currents and undertow with maximum values at mid depth (not shown). Wave periods had moderate influence on the velocity of SAG circulation cells (Fig. 8b). Although higher wave periods generated larger radiation stress gradients due to higher shoaling, the overall increase in the wave forcing and the remaining balancing terms (Supplementary Fig. 5b) was not significant compared to wave height (Supplementary Fig. 5a). When the wave reached the

steepness-breaking limit over the offshore end of the SAG profile, whitecapping resulted in changes to the velocity profile similar to the case of depth-induced breaking waves, but in this case the parabolic shape is less prominent due to lower vertical mixing.

Spur heights had significant influence in the strength of SAG circulation cells (Fig. 7b). Taller spurs were associated with stronger flows (Fig. 8c) due to the greater wave forcing (Supplementary Fig. 5c) as a result of higher waves

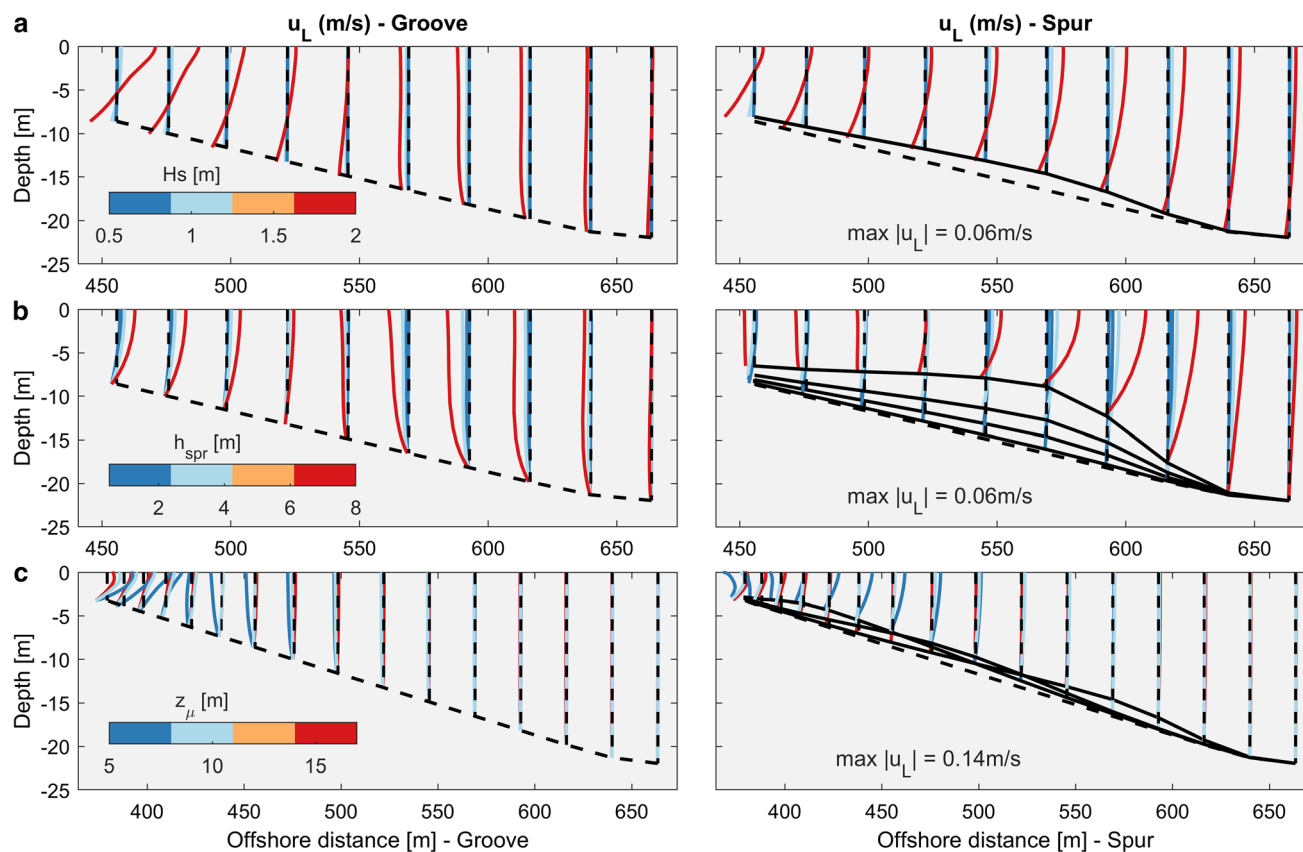


Fig. 7 Cross-shore variations in Lagrangian velocity, u_L , over the spur (right) and groove (left) for varying parameters. **a** Varying significant wave height H_s (0.5, 1 and 2 m). **b** Varying spur height h_{spr} (0.5, 2, 4 and 8 m). **c** Varying vertical position of maximum spur height z_μ (5, 10 and 17 m). The horizontal black lines represent the

bottom profile (solid for spur and dashed for groove). The vertical black lines indicate the positions where the cross-shore velocities are plotted; thus, velocities on these lines are null. The scales of the cross-shore Lagrangian velocities are given for each pair of spur and groove plots (i.e., a, b, and c), and are indicated in the right plots

over the spur and higher cross-shore and alongshore depth gradients. SAG wavelengths moderately influenced the strength of the flow, with longer SAG wavelengths resulting in higher SAG circulation cell velocities (Fig. 8d). For shorter SAG wavelengths, surface velocities over SAG on the lower fore reef were directed offshore (Fig. 3b); namely, the cell on the lower fore reef ceased to exist due to higher alongshore mixing of momentum (i.e., Reynolds stress horizontal gradients are larger for shorter wavelengths, see Supplementary Fig. 5d). Longer SAG wavelengths resulted in larger circulation cells that had proportionally higher alongshore currents, consistent with more mass flux within them. SAG formations with peak spur height occurring in shallower water (buttress type) had SAG circulation with higher velocities (Fig. 8i) due to higher wave forces (Supplementary Fig. 5i) situated in shallower waters. In addition, shallower spurs had circulation cells shifted onshore, with widening of the deeper cell (Fig. 7c). The reef slope for the more likely range ($\beta_f < 5^\circ$) where SAG formations are found did not

significantly influence either the strength or the shape of the velocity profile (Fig. 8f). Instead, the zonation of SAG circulation cells was affected, with steeper slopes providing wider circulation cells over the deeper portions of the SAG (not shown). The remainder SAG geometry parameters—the groove width (Fig. 8e), the reef flat widths (Fig. 8g), and the differential roughness between spur and groove (Fig. 8h)—had a minor role in the SAG hydrodynamics, which is consistent with nearly constant momentum terms occurring for the different input conditions (Supplementary Fig. 5e, g, h).

The degree of the alongshore dominance was directly proportional to the strength of the alongshore forcing (U_{10} , Supplementary Fig. 4j). In the cross-shore direction, the circulation cell on the upper fore reef was persistent, whereas the cell on the lower fore reef disappeared under alongshore forcing ($U_{10} \geq 5 \text{ m s}^{-1}$), thus having an effect similar to shorter SAG wavelengths (see Fig. 3b).

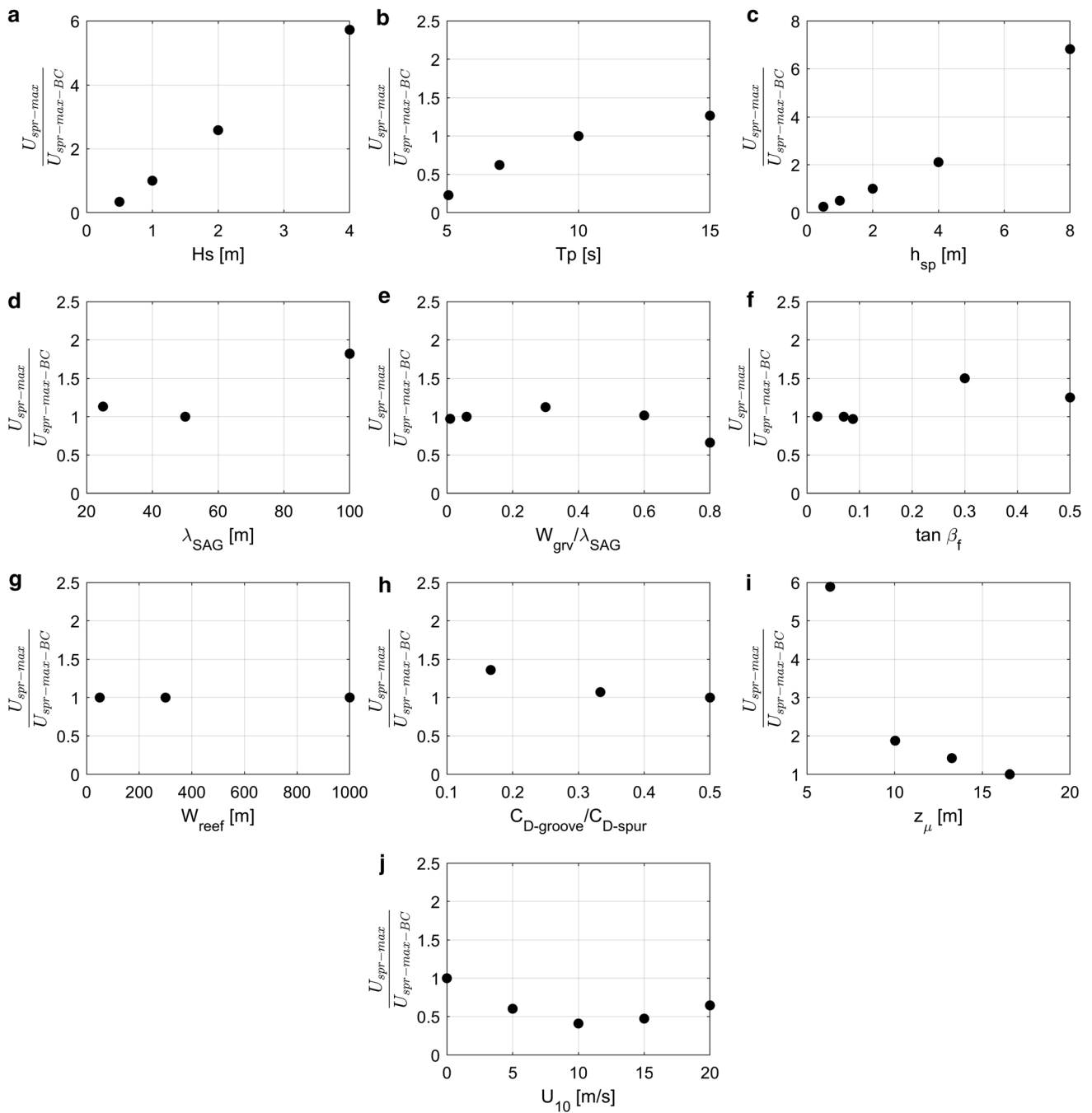


Fig. 8 Ratio of maximum offshore depth-averaged currents over the spur on the lower fore reef ($U_{spr-max}$) and its equivalent value for the base case ($U_{spr-max-BC}$) for varying forcing and spur-and-groove morphologic parameters. **a** Significant wave height, H_s . **b** Peak wave period, T_p . **c** Spur height, h_{spr} . **d** Spur-and-groove wavelength, λ_{SAG} .

e Ratio of groove width and SAG wavelength, W_{grv}/λ_{SAG} . **f** Spur-and-groove cross-shore slope, β_f . **g** Reef width, W_{reef} . **h** Ratio of friction coefficient between groove and spur, $C_{D-groove}/C_{D-spur}$. **i** Vertical position of maximum spur height, z_μ . **j** Alongshore wind speed, U_{10} . Note the varying scale on the y-axis in the different subplots

Compilation of velocity profiles shape

Here, we present the results of all simulations, including the runs for which the parameters H_s , T_p , h_{spr} , λ_{SAG} , and z_μ (i.e., the parameters associated with the largest changes in the flow strength, see section “Mechanisms and effects”)

were varied together, with the remaining model input parameters kept the same as the base case (Table 1). The results were evaluated in terms of the shape of the cross-shore SAG velocity profiles, and a classification of the velocity profile shapes into Types A, B, and C is proposed, as detailed below. These were found to reasonably

Table 2 Effect of waves, currents, and spur-and-groove geometry on the cross-shore velocity profiles over SAG and the associated forcing mechanisms.

Type	Parameter	Main effects	Mechanism
Wave parameters	H_{s0}	Significant enhancement of SAG circulation	Increase in all momentum terms for increasing H_s
		Reduction of offshore SAG circulation—wave-induced current profile with onshore flow near surface and undertow approaching the bottom	Depth-induced breaking
SAG geometry	$H_{s0} Lp_0^{-1}$	Reduction of offshore SAG circulation—wave-induced current profile with onshore flow near surface and undertow approaching the bottom	Steepness-induced breaking
	T_p	Enhancement of SAG circulation	Increase in all momentum terms for increasing T_p
	h_{spr}	Significant enhancement of SAG circulation	Increase in all momentum terms for increasing h_{spr}
	λ_{SAG}	Enhancement of SAG circulation	Increase in streamwise advective term for increasing λ_{SAG}
		Reduction of offshore SAG circulation by shifting of velocities towards offshore	Increase in Reynolds stress horizontal gradients for decreasing λ_{SAG}
Alongshore forcing	$\tan \beta_f$	Enhancement of SAG circulation	Increase in all momentum terms for increasing $\tan \beta_f$
	$C_{D-groove} C_{D-spur}^{-1}$	Reduction of offshore SAG circulation by shifting of velocities towards offshore	Decreasing in Reynolds stress vertical gradients over groove for decreasing $C_{D-groove} C_{D-spur}^{-1}$
	z_{qt}	Significant enhancement of SAG circulation	Increase in all momentum terms for decreasing z_{qt} (i.e., shallower)
	U_{10}	Reduction of offshore SAG circulation by shifting of velocities towards offshore	Increase in lateral advective term stresses for increasing U_{10}

represent the overall variation in cross-shore SAG velocity profile shape for all simulations.

The Type A flow pattern occurred for the base case (Figs. 3a and 5a, c), with offshore flow over spurs and onshore over grooves on the lower fore reef (Fig. 5a, b) that reversed on the upper fore reef (Fig. 5c). This includes both surface and depth-averaged flows over the groove and only depth-averaged flows over the spur. The alongshore and vertical flows were characterized by convergence towards the groove in the deeper portion of the lower fore reef (Fig. 5a) and a focalization towards the spur in the remainder of the fore reef up to the transition between lower and upper fore reef (Fig. 5b). After this transition, the alongshore currents were limited (Fig. 5c).

The Type B pattern had the same velocity profile shape over the spur as Type A (Figs. 3b and 5d–f). As for the groove, the flow on the upper fore reef for Type B was the same as Type A, with depth-averaged and surface offshore flows. The flow on the lower fore reef had an offshore surface flow, thus differing from Type A. The alongshore and vertical circulations were characterized by a convergence towards the groove (Fig. 5d–f and Supplementary Fig. 3d–f). The Type C flow pattern was defined as the flow profile for which wave breaking (i.e., steepness or depth-induced breaking) occurred, resulting in onshore flow close to the surface and offshore deeper in the water column (Fig. 3c).

Which flow pattern type occurred depended primarily on the interaction between the waves and the SAG bathymetry (i.e., whether waves broke or shoaled). With greater wave steepness ($H_{s0}L_{p0}^{-1}$), or with higher waves, there was greater potential for wave breaking, resulting in the Type C flow pattern. Apart from the breaking cases, SAG formations were characterized with Types A and B velocity profiles. The distinction between Types A and B was a function of the SAG wavelength, as Type B occurred over shorter SAG wavelengths. In Type B, surface velocities over SAG on the lower fore reef were directed offshore, due to the larger Reynolds stress horizontal gradients that were able to mix momentum between them (Supplementary Fig. 5d). Type A velocity profiles were the most common that occur with sufficiently large SAG wavelength and without wave breaking. Similarly, without wave breaking, at least the circulation cell on the upper fore reef—with offshore depth-averaged groove and onshore depth-averaged spur currents—was observed.

Discussion

Predicting the flow over SAG formations

Our study represents the first effort towards the description of the 3D hydrodynamics over a wide range of SAG geometries. Although our results corroborated the existence of counter-rotating, depth-averaged circulation cells previously reported by Rogers et al. (2013), the wave-driven flow over SAG formations is characterized by depth-varying velocities that were not previously elucidated. Consequently, a three-dimensional model as first utilized here is required for a complete understanding of the hydrodynamics and their implication to reef development.

Shoaling waves propagating over SAG were shown to drive Type A SAG circulation, which essentially consists of a two-cell system resulting in reversed depth-averaged current patterns over the spur and groove for different portions of the fore reef (i.e., one cell in the lower part and one cell in the upper portion). The velocity profiles are characterized by offshore-directed surface currents and onshore-directed bottom currents, except in the lower portion of the groove, where the currents are directed onshore. This circulation pattern is expected for all forcing conditions and SAG geometries with shoaling waves, except for the cases with alongshore forcing and with shorter SAG wavelengths. For these cases, the cell on upper fore reef still exists, but on the lower fore reef the currents over the SAG are directed offshore, except at the near-bottom where they reverse (Type B). When waves break over SAG, the velocity profile is characterized by onshore-directed surface currents, offshore-directed currents in the mid water column (i.e., undertow) and onshore-directed near-bottom currents (Type C).

Our results indicate that the circulation pattern over a SAG formation depends on both the SAG geometry and the incident forcing conditions occurring at a given time. The interdependency between the parameters makes the prediction of the velocity profile (i.e., among Types A, B, and C) a complex task. To demonstrate this, we took as examples the most important parameters associated with the strength of the flow, namely the wave and spur heights, and the depth at peak spur height. Although higher waves and spur heights, together with peak spur heights occurring in shallower waters, tend to result in stronger Type A circulation cells, Type C circulation occurs once waves start breaking.

The main influence of SAG wavelength seems to be the shift from circulation Types A to B for lower SAG wavelengths. The compilation of reported SAG structures by Duce et al. (2016) indicates that the mean SAG wavelengths (i.e., the average SAG wavelength on a single reef)

can vary between 20 and 200 m. Our results demonstrate the occurrence of Type B circulation for the majority of cases with a SAG wavelength of 25 m (i.e., the minimum value modelled), and for a few cases of 50 m, whereas all others SAG wavelengths had either Type A or Type C circulation when waves are breaking. Moreover, SAG wavelengths tend to increase with depth on a reef (Storlazzi et al. 2003; Duce et al. 2016). We hypothesize that a reef system with short SAG wavelengths (i.e., $\lambda_{\text{SAG}} < 50$ m) on the upper fore reef but with longer wavelengths on the lower fore reef would experience Type A circulation. However, because we used a schematic bathymetry with a constant (throughout a single reef) SAG wavelength in our study (see Fig. 1b, c and Appendix 1), the effect of varying SAG wavelengths within a single reef on the hydrodynamics remains unknown and warrants further investigation.

Another important factor for the prediction of the hydrodynamic over SAG is the presence of an alongshore forcing (such as alongshore wind-, tidally, or oblique wave-driven currents), which was shown to have two effects. First, alongshore forcing leads to the disappearance of the circulation cell on the lower fore reef, although the circulation on the upper fore reef remains regardless of the alongshore forcing (Type B). Second, our results indicate that, even with a relatively weak alongshore forcing (i.e., U_{10} of 5 m s^{-1}), the alongshore currents outstrip the relatively weak cross-shore currents (on the order of $1\text{--}10 \text{ cm s}^{-1}$) and the offshore circulation ceases to exist. Although the presence and strength of alongshore forcing is site- (e.g., reefs in micro and macro tidal environments) and time-specific (e.g., the occurrence of storms), it is reasonable to expect that at least some alongshore forcing occurs in the majority of situations (e.g., Rogers et al. 2015); thus, circulation Type B would predominantly be found worldwide.

The NFR13 measurements in Palmyra Atoll reported by Rogers et al. (2015) were predominantly characterized by offshore-directed surface currents and onshore-directed bottom-currents over the SAG, which resulted in depth-averaged offshore velocities over both (see Figs. 5a and 7; Rogers et al. 2015). As their measurements were taken in SAG formations with short SAG wavelengths and subjected to alongshore forcing, we infer that they experienced Type B of circulation, which meets this velocity profile shape in the lower portion of the reef (see Fig. 3b). As the measurements were limited to a single alongshore section of the SAG, a comparison at other locations of the reef profile (e.g., verification of the reversing of currents farther onshore) was not possible.

SAG in more energetic wave environments would likely result in wave breaking over deeper portions of the fore reef. Our results indicate that, for the cases with breaking,

the disappearance of the onshore circulation cell occurs, resulting in Type C circulation. The currents that result from depth-induced wave breaking are generally much stronger (order $\sim 10\text{--}100 \text{ cm s}^{-1}$) than those in the shoaling zone, which may have implications on sediment transport patterns (see section “[Implications of SAG hydrodynamics to reef development](#)”).

Overall, the prediction of the flow over SAG needs to consider specific sets of wave parameters, alongshore forcing, and SAG geometries because of their interdependency in affecting wave-induced flows. In addition, the type of circulation may vary both in time (i.e., depending on the forcing conditions) and in space (i.e., given the fact that SAG formations may vary within the same reef). Although our study provides general guidelines for forecasting flow pattern over SAG, we recommend in situ measurements and dedicated case study modelling (i.e., not schematic) for the study of the hydrodynamics over specific SAG formations.

Drivers of circulation

To get insight into the mechanisms by which SAG formations drive circulation, we modelled the flow over alongshore-uniform bathymetries (i.e., without SAG bathymetry and with alongshore-uniform friction). In the shoaling zone, offshore-directed surface currents and onshore-directed bottom velocities occur, which conceptually matches the velocity profile shape over the spur and over the upper portion of the groove. Therefore, the presence of onshore currents over the lower portion of the groove is the main change to the shape of the velocity profile associated with the presence of SAG. To verify the importance of the bottom friction as driver of circulation, we investigated the flow over alongshore-uniform bathymetries but with SAG friction (i.e., similar to the base case). The results were nearly similar to the alongshore-uniform bathymetries with uniform friction that had no SAG circulation. The main mechanism that causes distinct cross-shore current patterns over the spur and groove is the gradient in depth (and not the bottom friction), which was discussed by Rogers et al. (2013).

Our momentum balance analysis in the cross-shore direction indicated that the net of pressure gradient and wave force is the driver of flow, which was predominantly balanced by the Reynolds stress gradients in the water column and by friction at the bottom. In a depth-averaged sense, our results had similarities to the modelling of Rogers et al. (2013), as they also found the net of the pressure gradient and wave-force to drive the flow. However, they observed that this net is predominantly balanced by bottom friction, whereas we found that the Reynolds stress gradients, which were not part of their modelling

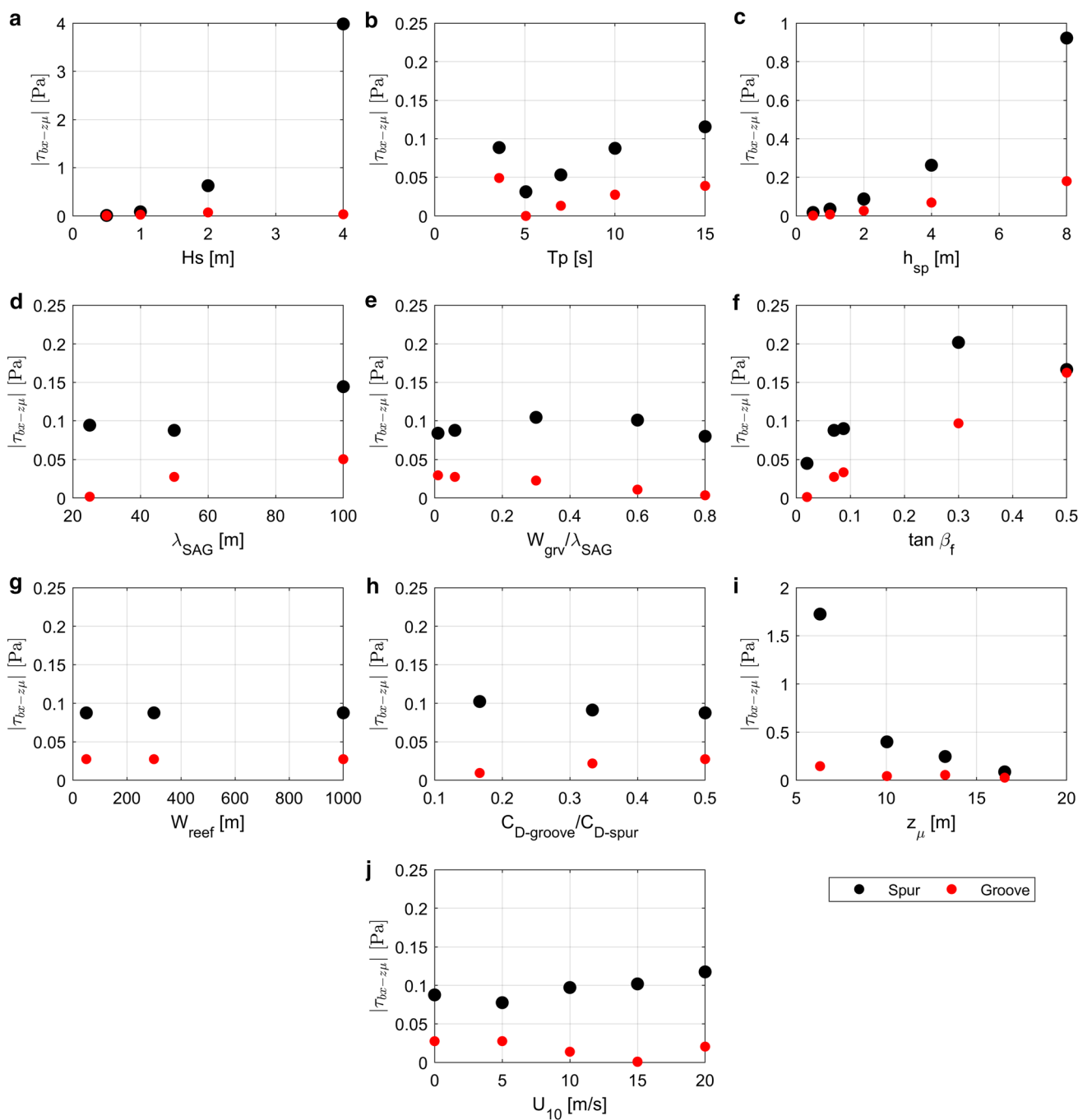


Fig. 9 Spur (black) and groove (red) cross-shore bottom shear stress at the depth at peak spur height ($\tau_{bx-z\mu}$) for varying forcing and spur-and-groove morphologic parameters. **a** Significant wave height, H_s . **b** Peak wave period, T_p . **c** Spur height, h_{sp} . **d** SAG wavelength, λ_{SAG} . **e** Ratio of groove width and spur-and-groove wavelength, W_{grv}/λ_{SAG} .

f Spur-and-groove cross-shore slope, β_f . **g** Reef width, W_{reef} . **h** Ratio of friction coefficient between groove and spur, $C_{D-groove}/C_{D-spur}$. **i** Vertical position of maximum spur height, z_{μ} . **j** Alongshore wind speed, U_{10} . Note the varying scale of the y-axis in the different subplots

(i.e., absent in the equation being resolved), to be relevant for the momentum balance.

In the estimation of the momentum terms in the cross-shore direction with the measurements in Palmyra Atoll, Rogers et al. (2015) found that the largest terms (i.e., with largest orders of magnitude) are the wave force, pressure

gradient, and lateral advective term. Although our results also found the two former to be the largest, the important role of the lateral advective term deviates from our findings. According to our results, the substantial increase in the lateral advective terms only occurs for the situations with alongshore forcing, for which they scaled with the net

of wave pressure gradient and wave force but had one order of magnitude less for each of them. We hypothesize that this increase in the measured lateral advective acceleration occurs due to the combined effect of greater alongshore forcing and alongshore spatial derivatives of the depth-averaged cross-shore velocity, which may occur for highly variable local bathymetries (i.e., in comparison with the idealistic, smooth bathymetries we adopted).

Implications of SAG hydrodynamics to reef development

The bottom shear stresses in the SAG zone were generally higher over the spur than over the groove (Figs. 4b and 9), which was also reported by Rogers et al. (2013, 2015). Accordingly, the potential for sediment transport would be higher over the spur and the groove. The bottom shear stresses over the spur would be able to bring fine sands (or smaller grain sizes) under suspension, whereas over the groove they could only move silts, as estimated with the Shields parameter for the base case bottom shear stresses at the depth at peak spur height (Figs. 4b and 9). In addition, the significant increase of bottom shear stresses for increasing wave height (Fig. 9a), spur height (Fig. 9c), and decreasing depth at peak spur height (Fig. 9i) only occurred over the spur, demonstrating that the difference in the potential for sediment transport over the spur and groove would increase for cases with stronger circulation (Fig. 8a, c, i). The relatively stronger alongshore currents over spurs (e.g., Rogers et al. 2015) would tend to transport sediment to the grooves, where they would more likely deposit due to lower shear stresses. Enhanced coral development over spurs would therefore be expected due to lower suspended sediment concentrations, unless extreme bottom shear stresses (e.g., during storms) occur, which could result in coral breakage (Storlazzi et al. 2005).

The cross-shore circulation pattern occurring for shoaling waves implies that bottom material (e.g., sediment) would be brought from the fore reef to the reef flat through the onshore-directed near-bottom currents (Fig. 4c). Although the bottom shear stresses are strong enough to suspend sediment like sands, we expect them to remain close to the seabed with the relatively weak currents in the SAG zone; thus, only the near-bottom currents would transport the sediment. Oppositely, the buoyant material near the surface (e.g., larvae, pollutants) would be transported from the reef flat to the fore reef through the offshore-directed surface currents (Fig. 4a). Together with the cross-shore currents, the vorticity associated with the secondary circulation (Fig. 5), which is concentrated over the spurs (Supplementary Fig. 3), may enhance mixing and, as such, increase the availability of food and nutrients to corals living over spurs. The occurrence of extreme events

(e.g., large wave heights) would likely result in breaking waves over the SAG. Accordingly, we expect the development of the Type C circulation with much higher velocities, which may suspend sediment higher up in the water column. With strong undertows (Type C circulation), sediment could be transported offshore across the SAG zone, promoting the recirculation of the sediment that is transported upslope during milder conditions.

The investigation of the mechanisms for the SAG development conducted by Duce et al. (2020) showed that both onshore (i.e., towards the reef flat) and seaward accretions over the spurs occurred in SAG formations. The onshore accretion is in agreement with all (Types A, B, and C) circulations modelled here, with onshore-directed, near-bottom velocities that increase upslope and shorewards. Seaward accretion does not seem to be supported by any of the near-bottom circulation patterns modelled here over the SAG zone. However, our results indicate that the near-bottom velocities quickly became directed offshore when waves start breaking close to the reef crest (not shown), which would result in an offshore-directed sediment transport and, as such, would match the seaward accretion. A detailed investigation of the sediment transport patterns across the whole reef profile is recommended to better understand how the hydrodynamics influence the SAG development.

Acknowledgements This material is based upon work supported by the U.S. Geological Survey's Coastal and Marine Hazards and Resources Program under Grant/Cooperative Agreement No. G14AC00396. The numerical model input files for this study can be found on ScienceBase at <https://doi.org/10.5066/P9ZRJ9H8>. We would like to thank the two anonymous reviewers for providing constructive reviews that improved this manuscript. Any use of trade, firm, or product names is for descriptive purposes only and does not imply endorsement by the U.S. Government.

Compliance with ethical standards

Conflict of interest On behalf of all authors, the corresponding author states that there is no conflict of interest.

Human and animal rights No animal studies were carried out by the authors for this article.

Appendix 1: Bathymetric and roughness schematization

To represent the vast variation of SAG formations, we used schematic bathymetries in the modelling. The conceptual bathymetry used here is equivalent to the idealized profile used by Rogers et al. (2013), which is based on 10 prominent SAG formations from areas with documented active coral growth on the southwestern coast of Moloka'i, Hawai'i. The shape of these SAG bathymetries was

simplified by a superposition of spurs on top of the reef profile, represented as a cosine function in the alongshore direction and a skewed Gaussian function in the cross-shore direction (Fig. 1), as shown below,

$$h(x, y) = h_{base} - h_{spr} h_x h_y, \quad (1)$$

where h is the depth, x is the cross-shore position, positive offshore, y is the alongshore position, $h_{base}(x)$ is the reef profile, h_{spr} is the spur height, and h_x and h_y are the cross-shore and alongshore SAG shape functions, as shown below,

$$h_x = \exp\left[-\frac{(x - \mu)^2}{2\varepsilon^2}\right], \quad (2)$$

$$h_y = \max\left[\left(1 + \alpha\right)\left|\cos\left(\frac{\pi y}{\lambda_{SAG}}\right)\right| - \alpha, 0\right], \quad (3)$$

where μ is the x for the maximum spur height, $\varepsilon(x)$ is a spreading parameter, with $\varepsilon = \varepsilon_1$ for $x \geq \mu$ and $\varepsilon = \varepsilon_2$ for $x < \mu$, λ_{SAG} is the SAG wavelength, and α is the coefficient for the alongshore shape which depends on the groove width (W_{grv}) and λ_{SAG} defined below,

$$\alpha = \frac{\left|\cos\left[\frac{\pi}{2}\left(1 + \frac{W_{grv}}{\lambda_{SAG}}\right)\right]\right|}{1 - \left|\cos\left[\frac{\pi}{2}\left(1 + \frac{W_{grv}}{\lambda_{SAG}}\right)\right]\right|}. \quad (4)$$

The spurs and grooves are oriented orthogonal to the shoreline, consistent with most of the reported SAG formations. Although the SAG cross-shore slope is highly variable in nature, a single slope between the depths of 0.5 (reef crest) and 22 m (offshore limit of model grid) was assumed for simplicity. Onshore, the reef flat is horizontal at a depth of 0.5 m, and the beach extends from -0.5 m to $+0.5$ m with a constant slope of $1/20$ (Fig. 1).

The hydrodynamic roughness across SAG is often highly variable, as spurs are covered by coral and algae, whereas grooves are often covered with sediment. A friction coefficient $C_{D-spr} = 0.06$ was used on the spurs for all simulations (e.g., Rosman and Hench 2011; Rogers et al. 2013). The ratio of friction coefficient between the spurs and grooves ($C_{D-grv} C_{D-spr}^{-1}$) was varied in the simulations to evaluate if the relative difference of roughness between spur and groove could drive circulation. In the mid position between the spurs and grooves, the friction values were assigned as proportional to $h_x h_y$ (i.e., the difference between the depth and the groove depth at the same alongshore section). Half of the roughness value between the spur and groove was assumed in the reef flat (i.e., $(C_{D-grv} + C_{D-spr})/2$).

Appendix 2: Validation

The assumption that applying SWAN without wave refraction and diffraction was appropriate was validated by comparing the wave field of SWAN with the wave-resolving, non-hydrostatic model SWASH that inherently accounts for shoaling, refraction and diffraction in its core equations (Zijlema and Stelling 2008). The validation cases consisted of runs similar to the sensitivity runs, with variations over the base case of five hydrodynamic and SAG geometry parameters, which are later shown to be dominant for the wave-induced flow pattern over SAG bathymetries: two wave parameters— H_s , T_p —, and three SAG geometrical parameters— h_{spr} , λ_{SAG} , and z_{μ} . Monochromatic shore-normal waves propagating over a set of two SAG formations were modelled, with alongshore cyclic boundaries, and the wave maker at a water depth of 22 m, similar to Rogers et al. (2013). Three vertical layers and a constant horizontal resolution of 1 m were used after sensitivity tests showed that with this set-up the wave dispersion is accurately represented.

A good agreement between SWAN and SWASH wave heights was obtained (Supplementary Fig. 2), showing that neglecting refraction and diffraction (SWAN) is a reasonable assumption for the calculation of waves over the SAG formations for which the difference between the wave height over the spur and groove is small. As only limited SAG wavelengths are considered in this work ($\lambda_{SAG} \leq 100$ m), we assumed this method was adequate for the current study.

References

- Andrews DG, McIntyre ME (1978) An exact theory of nonlinear waves on a Lagrangian-mean flow. *J Fluid Mech* 89(4):609–646
- Blanchon P, Jones B (1997) Hurricane control on shelf-edge-reef architecture around Grand Cayman. *Sedimentology* 44(3):479–506
- Booij N, Ris RC, Holthuijsen LH (1999) A third-generation wave model for coastal regions 1. Model description and validation. *J Geophys Res Oceans* 104:7649–7666
- Bouchon C (1981) Quantitative study of the scleractinian coral communities of a fringing reef of Reunion Island (Indian Ocean). *Mar Ecol Prog Ser* 4:273–288
- Buckley ML, Lowe RJ, Hansen JE, van Dongeren AR (2015) Dynamics of wave setup over a steeply sloping fringing reef. *J Phys Oceanogr* 42(12):3005–3023
- Dollar S (1982) Wave stress and coral community structure in Hawaii. *Coral Reefs* 1:71–81
- Duce S, Vila-Concejo A, Hamylton S, Bruce E, Webster JM (2014) Spur and groove distribution, morphology and relationship to relative wave exposure, Southern Great Barrier Reef, Australia. *J Coast Res* 70:115–120

- Duce S, Vila-Concejo A, Hamylton S, Webster J, Bruce E, Beaman R (2016) A morphometric assessment and classification of coral reef spur and groove morphology. *Geomorphology* 265:68–83
- Duce S, Dechnik B, Webster JM, Hua Q, Sadler J, Webb GE, Nothdurft L, Salas-Saavedra M, Vila-Concejo A (2020) Mechanisms of spur and groove development and implications for reef platform evolution. *Quat Sci Rev* 231:106155
- Falter JL, Atkinson MJ, Merrifield MA (2004) Mass-transfer limitation of nutrient uptake by a wave-dominated reef flat community. *Limnol Oceanogr* 49(5):1820–1831
- Goreau TF (1959) The ecology of Jamaican coral reefs, 1 - Species composition and zonation. *Ecology* 40:67–90
- Guilcher A (1988) Coral reef geomorphology. Wiley, Chichester
- Lesser GR, Roelvink JA, van Kester JATM, Stelling GS (2004) Development and validation of a three-dimensional morphological model. *Coast Eng* 51(8–9):883–915
- Lowe RJ, Falter JL (2015) Oceanic Forcing of Coral Reefs. *Ann Rev Mar Sci* 7:43–66
- Munk WH, Sargent MC (1948) Adjustment of Bikini Atoll to Ocean Waves. US Geol Sur Prof Paper 260 C, pp 275–280
- Odum HT, Odum EP (1955) Trophic Structure and Productivity of a Windward Coral Reef Community on Eniwetok Atoll. *Ecol Monogr* 25(3):291–320
- Quataert E, Storlazzi C, van Rooijen A, Cheriton O, van Dongeren A (2015) The influence of coral reefs and climate change on wave-driven flooding of tropical coastlines. *Geophys Res Lett* 42:6407–6415
- Rogers JS, Monismith SG, Feddersen F, Storlazzi CD (2013) Hydrodynamics of spur and groove formations on a coral reef. *J Geophys Res Oceans* 118:3059–3073
- Rogers JS, Monismith SG, Dunbar RB, Koweeck D (2015) Field observations of wave-driven circulation over spur and groove formations on a coral reef. *J Geophys Res Oceans* 120:145–160
- Rosman JH, Hench JL (2011) A framework for understanding drag parameterizations for coral reefs. *J Geophys Res* 116(C08025):1–15
- Shinn EA (1963) Spur and groove formation on the Florida reef tract. *J Sediment Petrol* 33:291–303
- Shinn EA, Hudson JH, Robbin DM, Lidz B (1981) Spurs and grooves revisited: construction versus erosion Looe Key Reef, Florida. Proceedings of the Fourth International Coral Reef Symposium. Vol. 1, Manila, pp. 475–483
- Silva RLCF (2017) Three-dimensional flow over spur-and-groove morphology. MSc thesis, Delft University of Technology
- Sneh A, Friedman GM (1980) Spur and groove patterns on the reefs of the northern gulfs of the Red Sea. *J Sediment Petrol* 50:981–986
- Storlazzi CD, Brown E, Field ME, Rogers K, Jokiel PL (2005) A model for wave control on coral breakage and species distribution in the Hawaiian Islands. *Coral Reefs* 24:43–55
- Storlazzi C, Logan J, Field M (2003) Quantitative morphology of a fringing reef tract from high resolution laser bathymetry: Southern Molokai, Hawaii. *GSA Bulletin* 115(11):1344–1355
- Weydert P (1979) Direction of growth of the spurs on an outer barrier reef tract - the example of the Grand Recif of Tulear (Madagascar). *Mar Geol* 30:9–19
- Wood R, Oppenheimer C (2000) Spur and groove morphology from a Late Devonian reef. *Sediment Geol* 133:185–193
- Zijlema M, Stelling GS (2008) Efficient computation of surf zone waves using the nonlinear shallow water equations with non-hydrostatic pressure. *Coast Eng* 55(10):780–790

Publisher's Note Springer Nature remains neutral with regard to jurisdictional claims in published maps and institutional affiliations.